ELSEVIER

Contents lists available at ScienceDirect

Materials & Design

journal homepage: www.elsevier.com/locate/matdes



Design optimization of lattice structures with stress constraints

Rossana R. Fernandes, Ali Y. Tamijani*

Embry-Riddle Aeronautical University, Daytona Beach, FL 32114, United States



HIGHLIGHTS

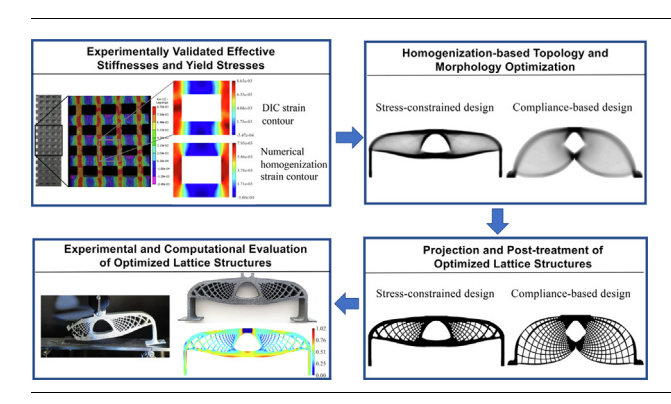
- Computational and experimental evaluations of effective mechanical properties.
- Homogenization-based stressconstrained optimization of lattice structures.
- Implementation of unit cell orthotropic properties in the optimization process.
- Experimental investigation of optimized lattice structure stiffnesses and strengths.

ARTICLE INFO

Article history: Received 4 June 2021 Revised 14 July 2021 Accepted 1 August 2021 Available online 3 August 2021

Keywords:
Topology optimization
Morphology optimization
Homogenization
Cellular solids
Additive manufacturing

G R A P H I C A L A B S T R A C T



ABSTRACT

This paper presents an experimentally validated framework used to perform topology and orientation (morphology) optimization of lattice structures subject to stress constraints. The effective stiffnesses and yield stresses of a unit cell are obtained using numerical homogenization and validated experimentally. Due to the orthotropic behavior of the unit cell, the modified Hill's yield criterion is used to describe the lattice strength. The effective orthotropic properties are implemented via macrostructure topology optimization to further improve the lattice structure stiffness. Homogenization-based optimization is performed using a coarse mesh and the optimized design is projected onto a fine mesh. This reduces the computational cost significantly. Finally, the projected design is post-processed to ensure the fabrication feasibility of the optimized lattice structure. The framework is tested for two cases: an L-shaped bracket and a single-edge notched bend (SENB) problem. A comparison of the compliance-based and stress-constrained designs used in the two cases demonstrates that the changes in the optimal material distribution that occur upon implementing the stress constraint result in higher yield strength. The SENB lattice structures are additively manufactured and the stiffnesses and yield strength of the optimized designs are compared to those obtained numerically.

© 2021 The Authors. Published by Elsevier Ltd. This is an open access article under the CC BY-NC-ND license (http://creativecommons.org/licenses/by-nc-nd/4.0/).

1. Introduction

A lattice structure comprises a network of cells with nodes and struts that offers exceptional properties such as high stiffness, energy absorption, and acoustic insulation. Lattice structure topol-

E-mail addresses: fernanr5@my.erau.edu (R.R. Fernandes), tamijana@erau.edu (A.Y. Tamijani).

ogy and morphology optimization have received considerable attention in recent years due to the emergence of new additive manufacturing techniques with the ability to fabricate microstructures. Among the various multiscale optimization methods used to design lattice structures, the homogenization-based approach has been investigated the most. This is because the effective properties of local microstructures can be obtained using homogenization theory. A surrogate model is then obtained for various microstructure densities, and this surrogate model is used within the opti-

^{*} Corresponding author.

mization process. This significantly reduces the computational complexity of microstructure analysis during the optimization procedure. Projection of homogenized designs is inspired by the work of Pantz and Trabelsi [1], in which the homogenized properties of rank-two laminates were used to optimize microstructure topologies and the principal direction was utilized to optimize cell morphologies. A mapping function based on the optimized orientation was needed to project the homogenized design. However, since the optimized orientation was symmetric with respect to π , a regularization approach was utilized to alleviate the discontinuities in the optimized orientation. Optimization was performed using a coarse mesh. The optimized design was projected onto a fine mesh using a mapping function and optimized density to generate the lattice structure. Later, each of the three steps i.e., homogenization, regularization, and projection was enhanced in other research studies. Groen and Sigmund [2] interpolated the homogenized properties of a square cell with rectangular hole instead of using the explicit homogenized properties of rank-two laminates. They also introduced a connected-component labeling approach to simplify regularization. Allaire, Geoffroy-Donders, & Pantz [3] addressed the conformality of square lattices. They also used an abstract manifold for the computational domain to reconstruct lattice structures from optimized homogenized designs.

Despite the success of stiffness-based de-homogenization approaches in generating lightweight periodic lattice structures, higher stiffnesses cannot be achieved if the stress constraints are not implemented within the optimization process and the optimized lattice structure fails. In addition, utilizing stress constraints may change the optimized lattice structure topology and morphology. There are three sources of complexity associated with stressconstrained optimization using homogenized properties: (1) stress singularities at zero density, (2) the large number of local stress constraints, and (3) the local nature of micro-stresses, which depends heavily on the cell micro-architecture. In the context of macrostructure topology optimization, stress singularities at zero density are addressed by using a polynomial, Kreisselmeier-Steinhauser, or reciprocal function to smooth the feasible design space [4.5]. The issue of large numbers of stress constraints has been addressed by aggregating the local constraints into a global constraint using the Kresselmeier-Steinhauser, p-norm, or pmean functions [6,7]. However, aggregations of stresses may not represent local stresses in structures. In order to preserve some of the local nature of the stresses while avoiding excessive computational cost, regional stress approaches have been proposed in which the design domain is split into several clusters and the stress constraints of the elements within each cluster are aggregated into a single constraint [8,9].

Unlike the above two issues, i.e., stress singularities and large numbers of local stress constraints, which exist in both macro and microstructural optimization, macrostructure optimization with microstructural stress considerations is less investigated. Microstructural stress constraints can be implemented within the macrostructure optimization process using two approaches: (a) finding the effective allowable stresses and (b) amplifying the homogenized stress. Cheng, Bai, and To [10] investigated topology optimization of lattice structures with stress constraints. A cubic lattice structure with a single-density design variable was considered. The Hill's yield criterion was used as the strength constraint. The effective yield strength in Hill's model was obtained by performing finite element analyses (FEAs) of lattice structures for various densities. Yu et al. [11] studied topology optimization of shelllattice structures with stress constraints. This study also used the Hill yield criterion. The effective yield strength was found for various densities. In both of these studies, a single design variable was employed to control the lattice structure topology. However, to use the full potential of the lattice structures in perpendicular directions, two variables must be used to describe the cell. To this end, Donders [12] studied minimization of the L2 norms of lattice structure stresses in square cells with rectangular holes using two variables. The effective stress was obtained using homogenized stress–strain relations. Then an amplification factor, which took micro-stress fluctuations into account, was multiplied by the effective stress to mimic the microstructural stress. While both stress amplification factor and effective allowable stress approaches were tested for microstructure topology optimization, cell orientations were kept unchanged in previous studies. However, various cells, such as square cells with rectangular holes that exhibit superior orthotropic properties, are weak with regard to withstanding shear stress. The orientation must be incorporated in the optimization process in order to take advantage of the orthotropic properties of the cell.

We previously studied compliance-based lattice structure topology and morphology optimization [13] using load paths and load flows as intermediate variables [14]. Later, we also studied optimization of material distribution and orientation and the subsequent projection for various types of cells and lattices using Fourier series representation [15]. The goal of the current study is to investigate the optimization of the topologies and morphologies of lattice structures that are subject to stress constraints. Square cells with rectangular holes with two characterizing parameters related to the void are used as the base cells. The effective unit cell stiffness and yield stress are obtained using numerical homogenization and compared to those found experimentally. Effective properties are obtained for various cell parameters in order to construct response surfaces. The response surfaces are implemented using a homogenization-based optimization algorithm. The modified Hill's criterion is implemented to establish the stress constraints and a material indicator variable is used to address the stress singularity issue. The stress constraints are represented using a p-mean function and a clustering approach is utilized to preserve some of the local nature of the stress. The optimized homogenized designs are then projected onto a fine mesh to generate the lattice structure. Finally, the projected lattice designs are post-processed to remove thin and floating members and enforce a minimum manufacturable feature size. The framework is tested for two cases: an L-shaped bracket and a singleedge notched bend (SENB) problem. Comparison of the compliance-based and stress-constrained designs for these cases clearly demonstrates that the optimized material distribution is different when the stresses are considered as constraints. In addition, the projected SENB design is additively manufactured and experimentally evaluated. The optimized design is shown to be manufacturable and to exhibit yield strength similar to those implemented via stress constraints. The four major contributions of this study are: (1) comparison of the effective stiffnesses and yield stresses obtained using numerical homogenization and experimental evaluation; (2) implementation of stress constraints and related sensitivity analyses in homogenization-based optimization of lattice structures; (3) incorporation of unit cell orthotropic properties in the optimization process to further improve the stiffness; and (4) demonstrating the fabrication feasibility of the lattice design and experimentally validating the optimized yield strength.

2. Effective cell properties

Square cells with rectangular holes are considered in the current study. As shown in Fig. 1, the cell is parameterized using two parameters (h_1 and h_2). The member thicknesses can be found using the corresponding parameter $t_n = 1 - h_n$ (n is the parameter number) and the corresponding cell volume fraction is $1 - h_1 h_2$.

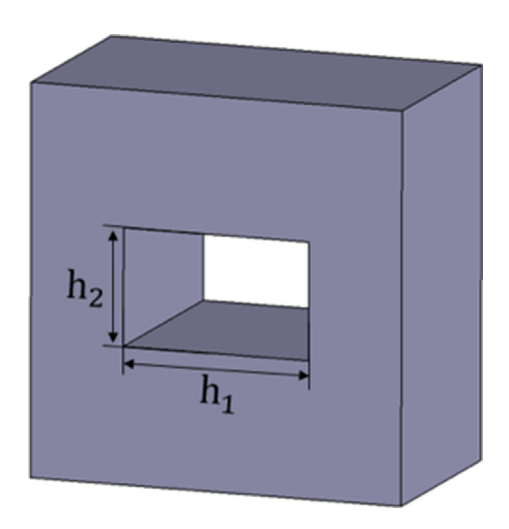


Fig. 1. Parameterization of a square cell with a rectangular hole.

The homogenized stiffness tensor (\bar{C}) is found via numerical homogenization [16–18] over a representative volume element (RVE):

$$\int_{Y} C_{ijpq} \left(\frac{\partial \chi_{p}^{kl}}{dy_{q}} - \varepsilon_{pq}^{(0)kl} \right) \frac{\partial \nu_{i}}{\partial y_{j}} dY = 0$$

$$\bar{C}_{ijkl}(\boldsymbol{r}) = \frac{1}{|Y|} \int_{Y} C_{mspq}(\boldsymbol{r}, \boldsymbol{y}) \left(\varepsilon_{pq}^{(0)kl} - \varepsilon_{pq}(\chi^{kl}) \right) \left(\varepsilon_{ms}^{(0)ij} - \varepsilon_{ms}(\chi^{ij}) \right) dY$$
(1)

where Y is the cell domain, $\varepsilon^{(0)kl}$ are the three macroscopic unit strains, χ^{kl} are the displacement fields, v_i is the virtual displacement field, and C is the stiffness tensor of the cell material. Using $\varepsilon_{pq}(\chi^{kl})$ allows the relation between the local micro-stress (σ) and effective macro-stress ($\bar{\sigma} = \bar{C} \ \bar{\varepsilon}; \bar{\varepsilon}$ is the effective strain) to be established [19]:

$$\boldsymbol{\sigma} = \boldsymbol{CM} \, \bar{\boldsymbol{S}} \, \bar{\boldsymbol{\sigma}}; M_{ijkl} = \frac{1}{2} \left(\delta_{ik} \delta_{jl} + \delta_{il} \delta_{jk} \right) - \varepsilon_{ij} (\boldsymbol{\chi}^{kl}) \tag{2}$$

where δ_{ij} is the Kronecker delta, M_{ijkl} is a local structure tensor that relates the effective strain and micro-strain [19], and $\bar{\bf S}$ is the inverse of the homogenized stiffness tensor. Since it is assumed that the cell is composed of an isotropic material, the von Mises criterion is chosen to describe the yield at the microstructure level. The von Mises yield criterion is expressed as

$$SR^{rs} \left(\left(\frac{\sigma_{22}^{rs}}{\sigma^Y} \right)^2 + \left(\frac{\sigma_{11}^{rs}}{\sigma^Y} \right)^2 - \frac{\sigma_{11}^{kl} \, \sigma_{22}^{rs}}{\sigma^{Y^2}} + \left(\frac{\sqrt{3} \, \sigma_{12}^{rs}}{\sigma^Y} \right)^2 \right) - 1 = 0 \tag{3}$$

where SR^{rs} in Eq. (3) represents the strength ratios and σ^{Y} is the material yield strength. The effective yield stress of the cell is obtained by multiplying the applied distributed load by the strength ratio. Four macroscopic unit distributed loads ($\sigma^{(0)rs}$; rs=11,22,12,44), including uniaxial in each direction, pure shear and hydrostatic, as shown in Fig. 2, are applied in order to obtain SR^{rs} . Since the unit distributed loads are applied, the macroscopic effective yield stresses ($\bar{\sigma}^{Y}$) are obtained based on the strength ratios

$$\bar{\sigma}_{rs}^{Y} = SR^{rs} \tag{4}$$

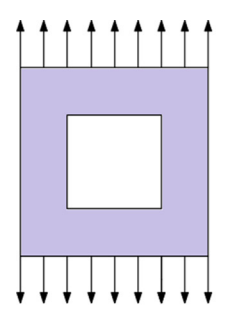
In order to validate the properties obtained using the homogenization method and evaluate the effect of the characterizing parameters on the effective tensile yield strength, 14×4 cell lattice structures were manufactured using an HP 3D High Reusabil-

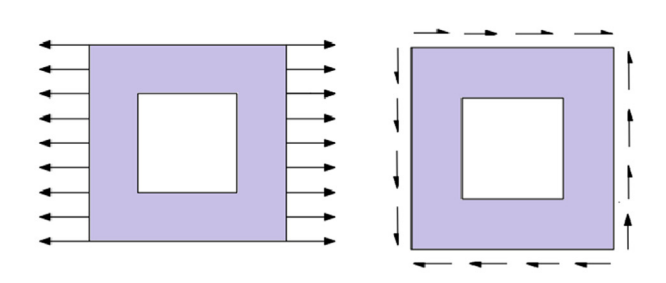
ity PA 12 in a Multi Jet Fusion (MJF) printer (HP Jet Fusion 5200 Series). Through the MJF, fusing and detailing agents were deposited along with heat onto thin layers of powder. This process was repeated until all layers were formed. The material properties were determined by testing five specimens according to ASTM D638-14. The Young's modulus of the material was $E=1288.30\pm45 MPa$; the yield strength was $\sigma^{\gamma}=18.3\pm0.9 MPa$, and the Poisson's ratio was $\nu=0.375\pm0.1$.

The lattice specimens were subjected to tensile loads using an MTS Criterion Model 43 test machine with a 50 kN load cell at a constant crosshead displacement rate of 0.875 mm/min. The test was terminated when the samples fractured fully. The strains were measured using digital image correlation (DIC). The square cell was 5mm long (L) and 3 mm thick. In the first set of experiments, $h_2 = 0.5L$ was kept constant and five different h_1 values $(h_1 = 0.1L, 0.3L, 0.5L, 0.7L \text{ and } 0.9L)$ were considered. In the other set of experiments, h₁ was kept constant at 0.5L and four different h_2 values ($h_2 = 0.1L, 0.3L, 0.7L$ and 0.9L) were considered. Table 1 shows the measured dimensions of the 3D printed samples. There is an average error of 2.42% between the CAD model and the printed sample. The results presented are the average of five samples that were 3D printed for each configuration. Fig. 3 (a) shows the printed model for cellular solid $h_1 = 0.7 L$ and $h_2 = 0.5 L$. The strain distribution for the middle of the sample was obtained via DIC and a single cell was extracted (Fig. 3 (b) and (c)). The results are compared to the distribution obtained via homogenization theory ($\varepsilon = MS \bar{\sigma}$) in Fig. 3 (d). The numerical homogenization contour shows that high strains appear around the hole with the highest strains near the four corners of the hole. In contrast, the experimental contour shows a high but more distributed strain on the side of the hole with the highest strain at the corner of the hole and expanding to the corner of the cell. Quantitatively, the experimental and numerical homogenization strains are within similar ranges. Fig. 3 (e)-(h) compares the experimental and computational strain contours for $(h_1=0.5L \text{ and } h_2=0.5L) \text{ and } (h_1=0.5L \text{ and } h_2=0.3L), \text{ for which }$ observations similar to those from $(h_1 = 0.7L \text{ and } h_2 = 0.5L)$ can be drawn.

Stress–strain curves are plotted for various h_1 values in Fig. 4 (a). All of the samples deform linearly before yielding. This is followed by nonlinear deformation and fracture. It is also observed that the strength and elastic modulus decrease as h_1 increases. A larger h_1 implies that a smaller area carries the load; this results in higher stresses. The stress–strain curves produced when h_2 varies (Fig. 4 (b)) exhibit trends similar to those noted when h_1 is allowed to vary, although the change in the yield strength is not as significant. The experimental and computational yield strength and elastic modulus of each sample are compiled in Table 2 and Table 3. The experimental yield stresses are determined from the 0.2% offset lines of the stress–strain curves (Fig. 4).

The difference between the numerical homogenization and experimental results is less than 16%. This validates the results obtained using the homogenization method. The largest difference of 15% is observed for $h_1=0.9L$ (Table 2). This can be attributed to geometric differences between the CAD model and the actual printed model. More specifically, the printer resolution forces the holes to be printed with some curvature instead of being completely rectangular. Rounded holes have lower stress concentrations. To compensate for this, a filtering technique based on the weighted average distance function [20] is applied to the homogenization results to remove concentrated stress from the corners of the holes. The effect of filter radius on maximum of micro-strain of unit cell is shown in Fig. 5. As can be seen, when there is no filtering, a high concentration in strain exists at the corners. However, this issue is alleviated when a filter radius above 0.05 is considered.





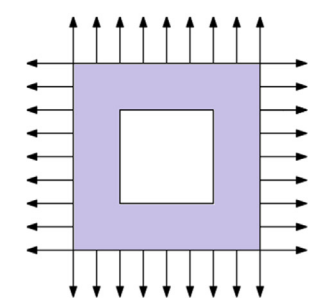


Fig. 2. Unit distributed loads applied to the representative volume element.

Table 1 Average measured dimensions of lattice specimens (width = 20mm, thickness = 3mm and L = 5mm).

	$h_1=0.1L\\$		$h_1=0.3L\\$		$h_1=0.5L\\$		$h_1=0.7L\\$		$h_1=0.9L\\$	
	Actual value	% error								
Width	19.85 ± 0.12	0.75	20.00 ± 0.02	0.02	20.03 ± 0.02	0.13	20.08 ± 0.03	0.38	20.13 ± 0.06	0.67
Thickn	3.06 ± 0.02	2.00	3.05 ± 0.03	1.56	3.03 ± 0.05	1.11	3.05 ± 0.02	1.56	3.06 ± 0.02	2.00
h_1	0.51 ± 0.04	2.00	1.54 ± 0.03	2.67	2.53 ± 0.02	1.20	3.56 ± 0.04	1.71	4.56 ± 0.04	1.41
h_2	2.52 ± 0.02	0.93	2.57 ± 0.04	2.57	2.57 ± 0.04	2.80	2.58 ± 0.03	3.07	2.49 ± 0.02	0.27
	$h_2=0.1L$		$h_2=0.3L$		$h_2=0.7L$		$h_2=0.9L$			
	Actual value	% error								
Width	20.06 ± 0.03	0.30	20.05 ± 0.07	0.27	20.06 ± 0.02	0.30	20.04 ± 0.06	0.20		
Thickn	3.01 ± 0.01	0.33	3.05 ± 0.03	1.67	3.08 ± 0.07	2.67	3.06 ± 0.08	2.11		
h_1	2.59 ± 0.14	3.47	2.61 ± 0.01	4.13	2.51 ± 0.04	0.40	2.52 ± 0.03	0.93		
h_2	0.53 ± 0.01	5.33	1.53 ± 0.03	2.22	3.62 ± 0.10	3.43	4.68 ± 0.16	3.93		

After experimental validation of the effective properties, properties were determined for various cell parameters and used to construct the response surfaces, $\bar{C}(h_n)$ and $\bar{\sigma}^{Y}(h_n)$, as shown in Fig. 6.

The homogenized stiffness matrix C is derived with respect to the principal axes of anisotropy. When the cell is rotated by angle θ , the stiffness matrix is updated using the transformation matrix (R):

$$\mathbf{C}_{\theta}(\theta, h_1, h_2) = \mathbf{R}(\theta) \mathbf{C}(h_1, h_2) \mathbf{R}^T(\theta)$$
(5)

It should be noted that the stress and strain tensors are expressed as vectors using Voigt notation. Due to the orthotropic behavior of the square cell with a rectangular hole, Hill's yield criterion is chosen to describe the lattice yield strength. It is assumed in Hill's yield criterion that the hydrostatic pressure does not affect the yield strength. However, this assumption is not accurate for lattice cells. Thus, a modified Hill's criterion [21] is utilized that includes the hydrostatic yield strength. The effective yield stresses $(\bar{\sigma}^{\rm Y})$ are used in the macroscopic modified Hill's yield criterion for each element:

$$\begin{split} F_{e} - 1 &= 0; F_{e} = \sqrt{\overline{\sigma}^{T}} \mathbb{V} \overline{\sigma} \\ \mathbb{V}_{11} &= \left(\frac{1}{\sigma_{11}^{Y}}\right)^{2} + \frac{1}{9} \left(\frac{1}{\sigma_{44}^{Y}}\right)^{2}, \mathbb{V}_{22} = \left(\frac{1}{\sigma_{22}^{Y}}\right)^{2} + \frac{1}{9} \left(\frac{1}{\sigma_{44}^{Y}}\right)^{2} \\ \mathbb{V}_{12} &= -\frac{1}{2} \left(\left(\frac{1}{\sigma_{11}^{Y}}\right)^{2} + \left(\frac{1}{\sigma_{22}^{Y}}\right)^{2} - \left(\frac{1}{\sigma_{33}^{Y}}\right)^{2} - \frac{2}{9} \left(\frac{1}{\sigma_{44}^{Y}}\right)^{2}\right), \mathbb{V}_{33} = \frac{1}{2} \left(\frac{1}{\sigma_{12}^{Y}}\right)^{2} \end{split}$$

$$(6)$$

The effective uniaxial, shear, and hydrostatic yield strengths $(\bar{\sigma}_{11}^Y, \bar{\sigma}_{22}^Y, \text{and } \bar{\sigma}_{12}^Y \text{ are, } \bar{\sigma}_{44}^Y)$ were found using Eq. (4). $\bar{\sigma}_{33}^Y$ is obtained from $\min(\bar{\sigma}_{11}^Y, \bar{\sigma}_{22}^Y)$. The yield criterion in Eq. (6) is developed in the

principal axes of anisotropy. The stresses and strains in the reference axes $(\bar{\sigma}_{\theta} \text{ and } \bar{\epsilon}_{\theta})$ are obtained using the transformation matrix (\mathbf{R}) .

3. Material models and stress constraints

As mentioned earlier, one issue related to stress constraints in topology optimization is that of stress singularities at low densities. This issue was first observed during a three-bar truss optimization [22]. It was shown that removing members is necessary to obtain a global minimum. However, the stress in a member increases as the member's thickness approaches zero. This prevents removal of the member. Several approaches to addressing this issue are discussed in the introduction section. The stress interpolation scheme [8] is adopted in this work. In order to establish the stress interpolation scheme, a material indicator variable (ϕ) is implemented. The material indicator has previously been used to obtain stiffness-optimized, coated structures with orthotropic infill [23]. In our work, the material indicator is used mainly to address the singularity issue during stress-constrained optimization. The stiffness matrix (\mathbf{C}_{θ}), density (ρ), and failure index (F_a^r) are updated using the material indicator variable:

$$\bar{\mathbf{C}}_{\theta}(\theta, h_1, h_2, \phi) = \phi^{q_1} \mathbf{R}(\theta) \, \bar{\mathbf{C}} (h_1, h_2) \mathbf{R}^T(\theta)
\rho = \phi (1 - h_1 h_2)
F_{\sigma}^r = \phi^{q_2} \sqrt{\bar{\sigma}^T} \mathbb{V} \, \bar{\sigma}$$
(7)

where q_1 and q_2 are parameters that penalize the intermediate density. Based on previous research [8,23], $q_1=3.0$ and $q_2=0.5$ are used in this work. The second challenge in stress-constrained topology optimization is related to the large number of stress constraints. To address this issue, the element failure index can be aggregated to a single constraint using the p-mean function. In order to preserve some of the local nature of the stress while avoid-

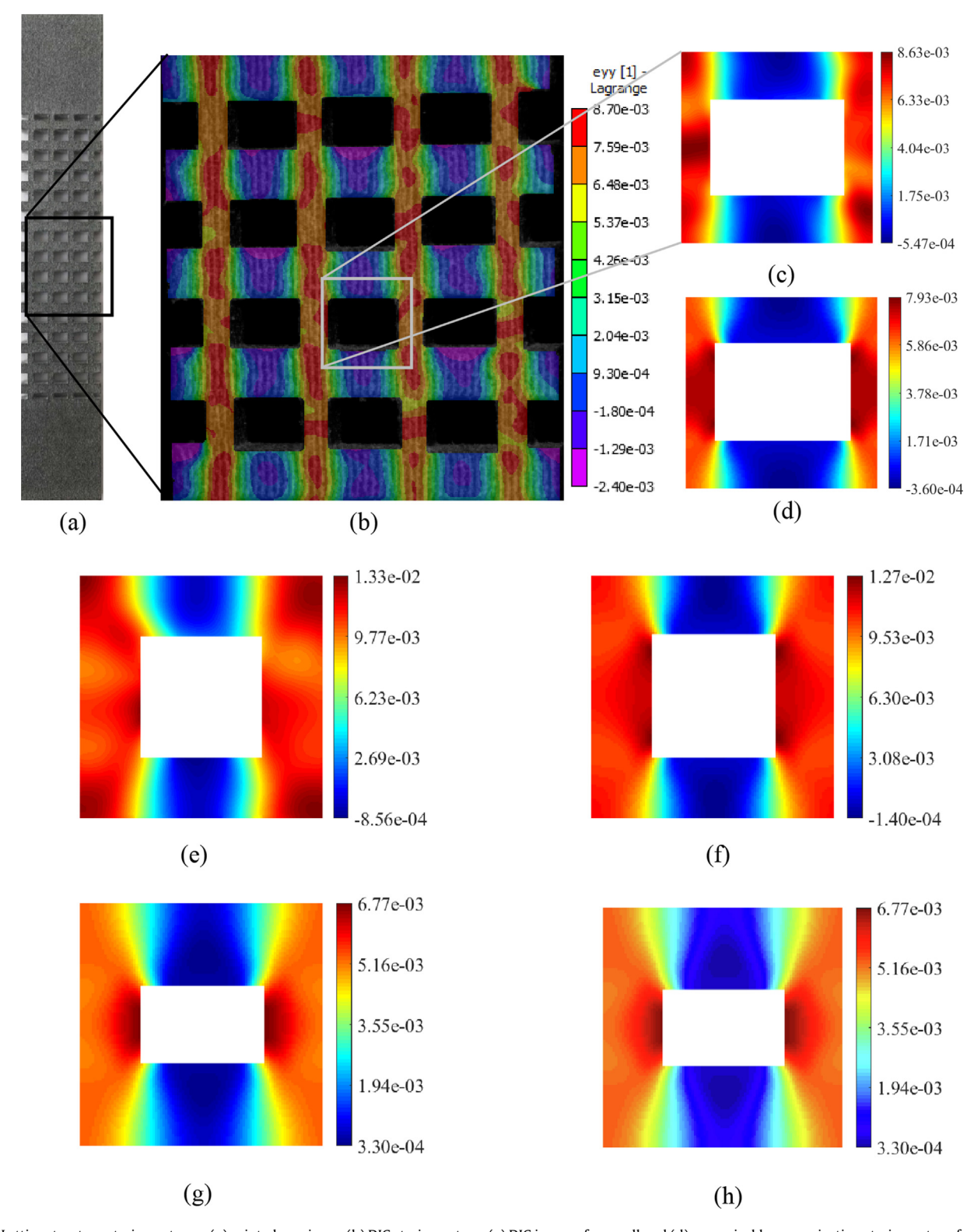
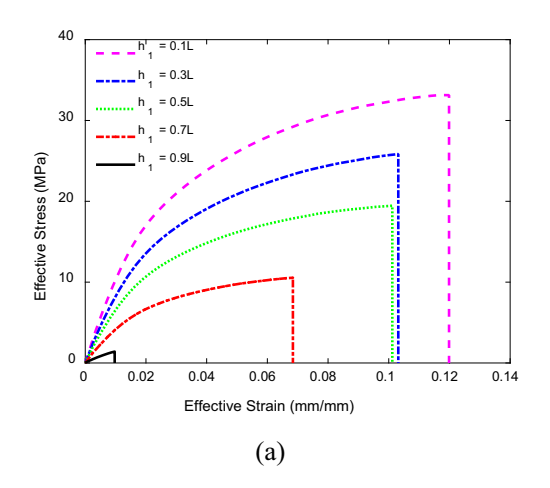


Fig. 3. Lattice structure strain contours: (a) printed specimen, (b) DIC strain contour, (c) DIC image of one cell and (d) numerical homogenization strain contour for $h_1 = 0.7L$ subjected to the distributed load of 2.98 N/mm^2 ; (e) DIC and (f) numerical homogenization strain contours of one cell with $h_1 = 0.5L$ subjected to the distributed load of 7.44 N/mm^2 ; (g) DIC and (h) numerical homogenization strain contours of one cell with $h_2 = 0.3L$ subjected to the distributed load of 3.98 N/mm^2 .

ing excessive computational cost, a clustering approach is utilized [8,24]. In the clustering approach, elements in the design domain are sorted based on their failure indexes. Then, the sorted elements are placed in N groups. The failure indexes of the elements in each group are aggregated into a single value using a p-mean function:

$$F_{m}^{p} = \left(\left(\frac{1}{\Omega_{m}} \right) \int_{\Omega_{m}} \left(F_{e}^{r} \right)^{p} d\Omega \right)^{\frac{1}{p}} \tag{8}$$

where m is the group number, Ω_m is the total volume of the elements in each group, and p is a tuning coefficient. Since the p-



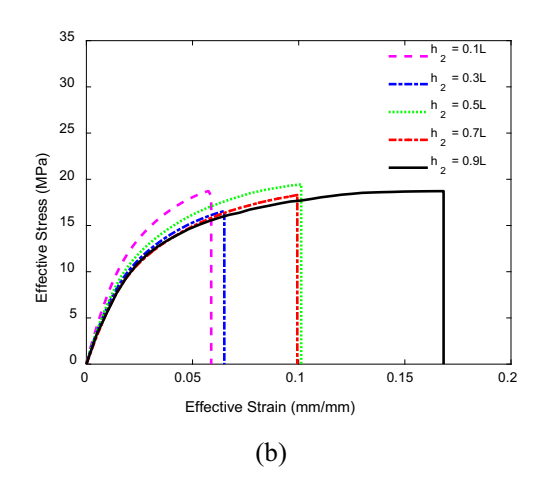


Fig. 4. Stress vs. strain curves: (a) variation with h_1 and (b) variation with h_2 .

 $\begin{tabular}{ll} \textbf{Table 2} \\ \begin{tabular}{ll} Variation in effective properties with h_1. \end{tabular}$

h ₁	0.1 L	0.3 L	0.5 L	0.7 L	0.9 L
Young's modulus varia	ation (MPa)				
Experimental	1105 ± 106.59	881 ± 30.85	728 ± 29.51	453 ± 11.09	178 ± 6.27
Numerical	1188	945	702	448	172
% Difference	7.24	6.97	3.63	1.00	3.70
Yield strength variatio	n (MPa)				
Experimental	14.93 ± 2.80	12.17 ± 1.18	9.3 ± 0.66	5.77 ± 0.81	1.55 ± 0.37
Numerical	14.5	11.05	8.27	5.33	1.8
% Difference	2.94	9.62	11.72	7.87	15.14

Table 3 Variation in effective properties with h₂.

h_2	0.1 L	0.3 L	0.5 L	0.7 L	0.9 L
Young's modulus varia	ation (MPa)				
Experimental	886 ± 33.16	700 ± 37.34	728 ± 29.51	642 ± 45.47	632 ± 51.25
Numerical	840	757	702	668	652
% Difference	5.34	7.79	3.63	4.00	3.16
Yield strength variatio	n (MPa)				
Experimental	11 ± 0.4	8.97 ± 0.15	9.30 ± 0.66	8.33 ± 0.29	8.43 ± 0.38
Numerical	9.71	8.35	8.27	8.15	8.1
% Difference	12.46	7.12	11.72	2.22	4.03

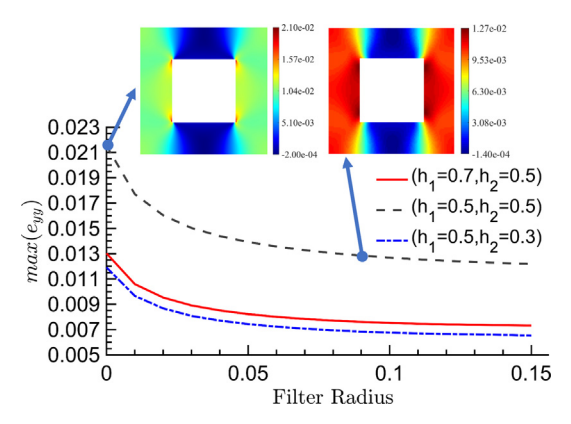


Fig. 5. The effect of filtering radius on maximum of micro-strain.

mean function in Eq. (8) converges to a lower value of $\max(F_e)$, a scaling factor (s) is implemented during each iteration to decrease the difference between the p-mean function and the $\max(F_e)$ [8]:

$$g_{m} = s_{m}^{k} F_{m}^{P} - 1; s_{m}^{k} = \alpha^{k} \frac{\max(F_{e}^{r})^{k-1}}{\left(F_{m}^{P}\right)^{k-1}} + (1 - \alpha^{k}) s_{m}^{k-1}$$
(9)

where g_m is the stress constraint for each group. The parameter α^k is selected based on the s_m^k in two consecutive iterations; $\alpha^k = 0.5$ if s is oscillating, otherwise $\alpha^k = 1.0$.

4. Topology and morphology design optimization algorithms

In each optimization iteration, the topology and morphology optimizations are performed in two steps. The characteristic parameters and material indicator variable are optimized in the first step and the optimized cell orientation is obtained in the second step. Two topology optimization problems are considered in this research: (1) minimizing the compliance (maximizing stiffness) subjected to the equilibrium equation and volume constraint (V_g) , and (2) minimizing the volume subjected to the equilibrium equation and stress constraints. For the compliance optimization problem, we start with initial variables (h_1^k, h_2^k, ϕ^k) , and θ^k for

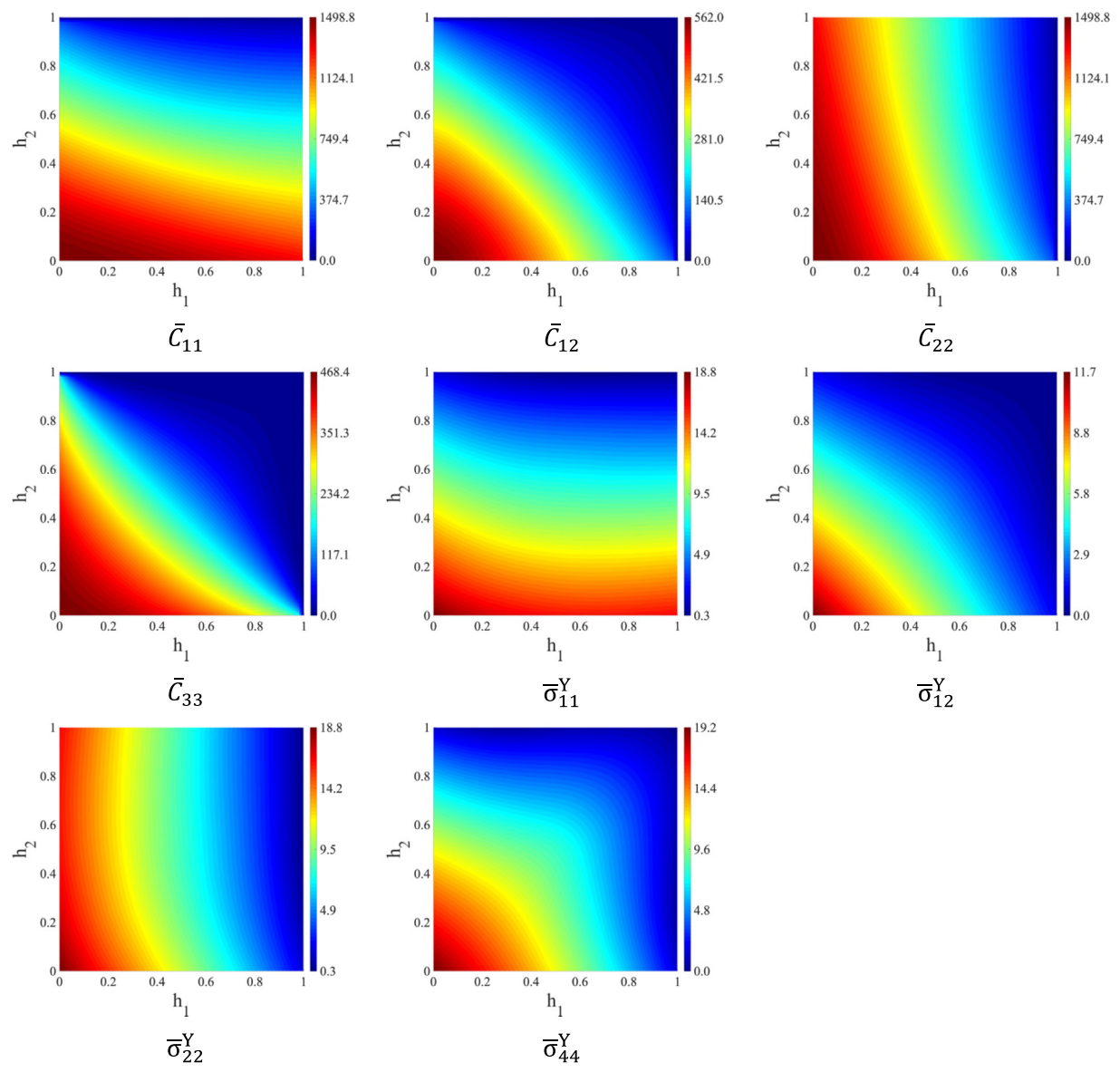


Fig. 6. Response surfaces for the homogenized stiffness (MPa) and yield strength (MPa).

k=0) and perform the following steps during each optimization iteration:

- (a) Find $\bar{\boldsymbol{C}}(h_1^k, h_2^k)$.
- (b) Solve the elasticity problem, KU = F, where K, U, and F are the stiffness matrix, the displacement vector, and the force vector, respectively.
- (c) Filter the design variables h_1^k, h_2^k , and ϕ^k
- (d) Obtain the sensitivity of the objective function and constraint with respect to the design variables h_1^k, h_2^k, ϕ^k , and θ^k .
- (e) Perform topology optimization (10) and update \boldsymbol{h}_{n}^{k+1} and $\boldsymbol{\phi}^{k+1}$.
- (f) Perform morphology optimization (11) and update θ^{k+1} .
- (g) The process continues (k = k + 1) until convergence.

subjected to
$$(\frac{1}{V_0})\int_{\Omega}\rho d\Omega - V_g \leq 0$$
 (10) design variables $0 < h_n$ and $\phi \leq 1$. $n=1, 2$

$$\min SE/SE_0 + P_\theta/2P_{\theta 0}$$
design variables $-2\pi \le \theta \le 2\pi$ (11)

where SE is compliance $\left(SE = \bar{\boldsymbol{\varepsilon}}^T \bar{\boldsymbol{C}} \; \bar{\boldsymbol{\varepsilon}}\right)$, and SE_0 is the compliance in the first iteration. V_0 is the volume of the design domain, and V_g is the volume fraction constraint. P_{θ} is a control function that penalizes sudden changes in orientation among neighboring elements and $P_{\theta 0}$ is the penalty function in the first iteration [25]:

$$P_{\theta} = \sum_{e=1}^{ne} \sum_{i=1}^{f} \left(\frac{1}{2} - \frac{1}{2} \cos(4\theta_{e} - 4\theta_{i}) \right)$$
 (12)

where f is the number of elements connected to the element e. The topology optimization problem presented in (10) is solved using the method of moving asymptotes [26]. The morphology optimization problem (11) is solved using the Broyden–Fletcher–Goldfarb–Shan no (BFGS) algorithm from the open-source library NLopt [27]. The stress-constrained optimization steps are similar to those from compliance optimization, but incorporate the following changes:

 $\mathbb{V}\left(h_1^k, h_2^k\right)$ is also calculated in step (a) and topology optimization with stress constraints (13) is performed in step (e).

$$\begin{aligned} \min V_f &= (\frac{1}{V_0}) \int_{\Omega} \rho d\Omega \\ \text{subjected to } F_m^p - 1 &\leq 0 \\ \text{design variables } 0 &< \pmb{h}_0 \text{ and } \pmb{\phi} \leq 1. \quad n = 1,2 \end{aligned} \tag{13}$$

The sensitivity analyses for the compliance objective function, stress constraints, and volume fraction constraint are required in the optimization process. The sensitivity of the volume fraction is:

$$\frac{\frac{d}{dh_{1e}} \int_{\Omega} v d\Omega = -\phi h_{2e} \Omega_{e}$$

$$\frac{d}{dh_{2e}} \int_{\Omega} v d\Omega = -\phi h_{1e} \Omega_{e}$$

$$\frac{d}{d\phi} \int_{\Omega} v d\Omega = (1 - h_{1e} h_{2e}) \Omega_{e}$$
(14)

where Ω_e is the area of each element. The sensitivities of the compliance and p-mean stress measure are obtained using the adjoint method. The compliance objective function is self-adjoint and its sensitivity is:

$$\frac{dSE}{dh_{ne}} = -\phi^{q_1} \bar{\boldsymbol{\varepsilon}}^T \frac{d\bar{\boldsymbol{c}}}{dh_{ne}} \bar{\boldsymbol{\varepsilon}} \Omega_e;$$

$$\frac{dSE}{d\phi_e} = -q_1 \phi^{(q_1-1)} \bar{\boldsymbol{\varepsilon}}^T \bar{\boldsymbol{C}} \bar{\boldsymbol{\varepsilon}} \Omega_e;$$

$$\frac{dSE}{d\theta_e} = -2\phi^{q_1} \bar{\boldsymbol{\varepsilon}}^T \bar{\boldsymbol{C}} \frac{d\mathbf{R}^T}{d\theta_i} \bar{\boldsymbol{\varepsilon}}_{\theta} \Omega_e$$
(15)

The sensitivity analysis of the p-mean stress measure is obtained using Eq. (8):

$$\frac{dF_{m}^{p}}{dh_{ne}} = \left(-\phi^{q_{1}} \boldsymbol{\varepsilon} (\boldsymbol{\lambda}_{m}^{T}) \boldsymbol{R} \frac{d\bar{\boldsymbol{C}}}{dh_{ne}} \bar{\boldsymbol{\varepsilon}} + \frac{\left(F_{m}^{p}\right)^{1-p}}{2\Omega_{e}} (F_{e}^{r})^{p-1} \left(\frac{\phi^{q_{2}}}{F_{e}}\right) \right) \times \left(2\bar{\boldsymbol{\sigma}}^{T} \boldsymbol{\nabla} \frac{d\bar{\boldsymbol{C}}}{dh_{ne}} \bar{\boldsymbol{\varepsilon}} + \bar{\boldsymbol{\sigma}}^{T} \frac{d\boldsymbol{\nabla}}{dh_{ne}} \bar{\boldsymbol{\sigma}}\right) \Omega_{e} \tag{16}$$

$$\frac{dF_{m}^{p}}{d\phi_{e}} = \left(-q_{1}\phi^{q_{1}-1}\boldsymbol{\varepsilon}(\boldsymbol{\lambda_{m}^{T}})\boldsymbol{R}\bar{\boldsymbol{c}}\bar{\boldsymbol{\varepsilon}} + \frac{\left(F_{m}^{p}\right)^{1-p}}{2\Omega_{e}}(F_{e}^{r})^{p-1}q_{2}\phi^{q_{2}-1}F_{e}\right)\Omega_{e}$$

where the adjoint variables are:

$$\lambda_{\mathbf{m}}^{\mathbf{T}} \mathbf{K} = \mathbf{F}_{\mathbf{m}}^{a}$$

$$\mathbf{F}_{\mathbf{m}}^{a} = \sum_{e \in \Omega_{m}} \int_{\Omega_{e}} \frac{\left(\mathbf{F}_{e}^{p}\right)^{1-p}}{\Omega_{m}} \left(\mathbf{F}_{e}^{r}\right)^{p-1} \left(\frac{\phi^{q_{2}}}{F_{e}}\right) \left(\bar{\boldsymbol{\sigma}}^{T} \mathbb{V} \, \bar{\boldsymbol{C}} \, \boldsymbol{R}^{T} \boldsymbol{B}\right) d\Omega_{e}$$

$$(17)$$

The topology and morphology optimization framework are developed using the open-source PDE solver FreeFem++ [28]. P_1 -functions are utilized to discretize the displacements and adjoint variables and P_0 -functions are implemented to discretize all other variables, such as stress, strain, characteristic parameters, the material indicator variable, and orientation. In order to regularize the characteristic parameters and material indicator variable, the Helmholtz-type filtering approach is adopted in this research [29]:

$$-\left(\frac{r_f}{2\sqrt{3}}\right)^2 \nabla^2 \overset{\sim}{h_n} + \overset{\sim}{h_n} = h_n \quad \text{on} \quad \Omega \stackrel{\widetilde{\partial h_n}}{\partial \Gamma} = 0 \quad \text{on} \quad \partial \Gamma$$
 (18)

where r_f is the filter radius, Ω is the design domain, $\partial \Gamma$ is the boundary of the design domain, and $\stackrel{\sim}{h}_n$ is the intermediate filtered

variable. P_1 -functions are used to discretize h_n , which is then transformed into a P_0 -function to obtain the filtered characteristic parameters. The same procedure is applied to obtain the filtered material indicator variable (ϕ). In addition, a smoothed Heaviside projection [30] is applied to the material indicator variable to produce the 0/1 design variable:

$$\bar{\phi} = \frac{\tanh(\beta \eta) + \tanh\left(\beta \left(\phi - \eta\right)\right)}{\tanh(\beta \eta) + \tanh\left(\beta \left(1 - \eta\right)\right)},\tag{19}$$

where β is the projection parameter used to control the intensity of the projection. The parameter η specifies the inflection point and is set to $\eta=0.5$. It was previously shown that use of homogeneous Neumann boundary conditions in the filtering formulation may cause several issues in the optimized design, such as forcing structural members to be perpendicular to the boundary [31]. A boundary padding approach is suggested to address this issue [31,32]. In the padding technique, the boundary of the design domain is extended by a width equal to the filter radius, except at the support and load. This approach is adopted in the current research to address the boundary effects of Helmholtz-type filtering.

The material properties, state variables, and objective and constraint functions are obtained using the projected material indica-

tor variable ϕ and filtered characteristic parameters h_n . In order to retrieve the sensitivities of the objective and constraint functions (f) with respect to the design variables ϕ and h_n , the following chain rules are implemented [29,30]:

$$\frac{\partial f\left(\stackrel{\leftarrow}{\mathbf{h}}_{\mathbf{n}}\right)}{\partial \mathbf{h}_{\mathbf{n}}} = \frac{\partial f}{\partial \stackrel{\leftarrow}{\mathbf{h}}_{\mathbf{n}}} \frac{\partial \stackrel{\leftarrow}{\mathbf{h}}_{\mathbf{n}}}{\partial \mathbf{h}_{\mathbf{n}}}
\frac{\partial f\left(\stackrel{\leftarrow}{\boldsymbol{\phi}}\right)}{\partial \boldsymbol{\phi}} = \frac{\partial f}{\partial \stackrel{\leftarrow}{\boldsymbol{\phi}}} \frac{\partial \stackrel{\leftarrow}{\boldsymbol{\phi}}}{\partial \stackrel{\leftarrow}{\boldsymbol{\phi}}} \frac{\partial \stackrel{\leftarrow}{\boldsymbol{\phi}}}{\partial \boldsymbol{\phi}} \tag{20}$$

Compliance-based and stress-constrained topology and morphology optimization are applied to an L-bracket problem. The dimensions and boundary conditions for the L-shaped bracket problem, including the clamped top edge and distributed load applied to the right corner ($F = 1000 \ N/cm$) are shown in Fig. 7. The load is distributed over 0.1cm and a region with an area of 0.2×0.2 cm² near the applied load is excluded from the design domain. The domain is discretized using 23,544 triangular elements. The filter radius is 0.2cm and the maximum value of the projection parameter is $\beta = r_f / \sqrt{3} l_e$ [33], where l_e is the minimum elemental edge length ($l_e = 0.033$ cm) in this study. As suggested in [33], β is updated every 100 iterations until it reaches the maximum value. The response surfaces (Fig. 6) are used to obtain homogenized properties \boldsymbol{c} and $\bar{\sigma}^{Y}$ during optimization. First, the stress-constrained optimization is performed. Ten regional stress constraints (m = 10) and a p-mean parameter of p = 10 are selected. The optimized volume fraction, compliance, and maximum of the failure index are reported in Table 4. The convergence histories for the volume fraction and maximum failure index are shown in Fig. 8. The optimized material distribution

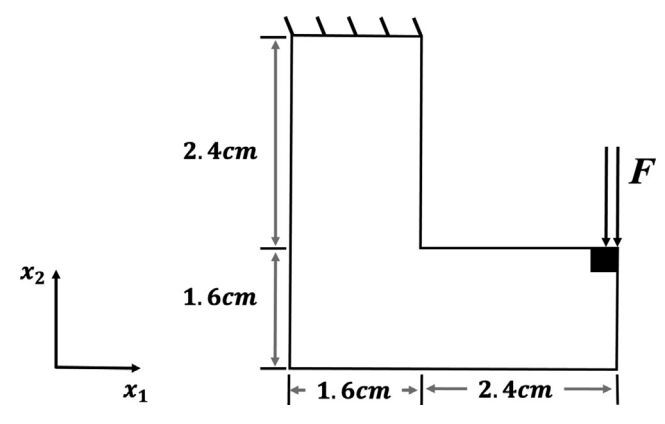


Fig. 7. Dimensions and boundary conditions for the L-shaped bracket test case.

Table 4
L-bracket optimized design volume fractions, compliances, and maximum of failure index

Optimization Problem	V_f	SE (Ncm)	$\max(F_e^r)$
Stress-constrained optimization	33.6%	28	1.0
Compliance-based optimization	33.6%	20	3.1

 $(\rho=\bar{\phi}(1-h_1\,h_2))$, orientation, and failure index are shown in Fig. 9 (a), (b), and (c), respectively. As shown in the figure, the material at the re-entrant corner is removed during the topology optimization process, the failure index is uniformly distributed, and the stress constraint is satisfied. Next, the compliance-based optimization problem with volume fraction constraints is considered. The upper bound of the volume fraction is taken as the optimized volume fraction of the stress-constrained optimized design ($V_g=33.6\%$). Upon comparing the material distributions and failure indexes of the two optimization problems in Fig. 9, it is evident that the stress constraint is not satisfied in the compliance-based design because of the stress concentration at the right-angle corner of the design. The results presented in Table 4 show that lower compliance is obtained by using compliance optimization for the same volume fraction.

5. Projection and post-treatment of lattice structures

The homogenized design presented in Fig. 9 is obtained based on the assumption of an infinitesimal length scale. The projection of the homogenized design to a finite length scale is discussed in this section. As shown in [15,34], a cellular solid can be represented by Fourier series expansions. For the square cell with a rectangular hole considered in this research, implementing two cosine terms is sufficient to represent the lattice structure [1]:

$$\Omega_{\mathsf{M}} = \{ (x_1, x_2) \in D | \cos\left(\frac{2\pi\psi_1(x_1, x_2)}{\Lambda}\right) \\
> \cos(\pi\phi(1 - h_1)) \cup \cos\left(\frac{2\pi\psi_2(x_1, x_2)}{\Lambda}\right) \\
> \cos(\pi\phi(1 - h_2)) \} \tag{21}$$

where Λ is the periodicity parameter and ψ_n is the mapping function used to project the homogenized design. The mapping functions are obtained using the optimized orientation $(\boldsymbol{v} = [\cos(\theta), \sin(\theta)])$ [3]:

$$\nabla \psi_1 = \mathbf{e}^{\gamma} \boldsymbol{v} \tag{22}$$

where γ is a dilatation factor used to adjust the lattice spacing [3]:

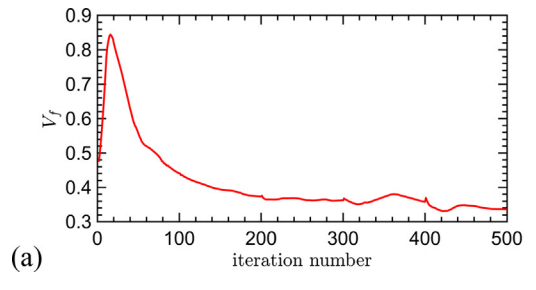
$$\nabla \gamma = (-\nabla \times \boldsymbol{v}) \, \bar{\boldsymbol{v}} + \left(\nabla \times \bar{\boldsymbol{v}}\right) \boldsymbol{v} \tag{23}$$

and $\bar{\boldsymbol{v}}$ is a vector that is perpendicular to \boldsymbol{v} . The mapping function ψ_2 can also be obtained by using Eq. (22) and changing \boldsymbol{v} to $\bar{\boldsymbol{v}}$. How-

ever, the mapping functions fail to produce the projected lattices due to irregularities in the optimized orientation (see Fig. 9 (b) and (e)). In order to create a locally continuous vector field, we adapted the vector field combing suggested in [35]. In this procedure, we start with an element in the lower left corner, the element is added to the visited element vector (i), the adjacent element (e) with minimum x_2 (see Fig. 7) is selected, and the following function is calculated for four possible frame orientations (j), including $(0, \pi, \pi/2, -\pi/2)$:

$$R_e^i = \sum_i (1 - \boldsymbol{v}_i.\boldsymbol{v}_e) \tag{24}$$

The best frame orientation occurs at minimum of R_{ρ}^{j} . The element (e) is then added to the visited vector and the next adjacent element is considered. While following this procedure does not ensure that singularities are prevented, they occur only in the void or solid region and not in the area with intermediate density for the test cases considered in this research. After combing procedure. the mapping functions are obtained using Eq. (22) and the homogenized design is projected using Eq. (21). The projected design for the periodicity parameter $\Lambda = 0.065$ is shown in Fig. 10 (a). Postprojection treatment must be implemented to ensure the manufacturability of the optimized designs. Details of the post-processing framework are discussed in our previous work [15]. A summary of the process is outlined here. The process consists of five steps: 1) implementing the minimum feature size; 2) enforcing the density threshold; 3) imposing the density boundary; 4) removing small holes; and 5) eliminating floating members and smoothing boundaries. Within the first step, the cell size is defined based on the modified periodicity ($t_f = \Lambda e^{-\gamma}$ [3]), which is plotted in Fig. 10 (b). Cells smaller than $2h_{min}$ ($h_{min} = 0.3\Lambda$ is selected for the L-bracket projected designs) are identified and two conditions are used to ensure that all features are greater than the minimum threshold (h_{min}). Small cells (t_f < $2h_{min}$) in the region $\rho \leq 0.5$ are removed $(1 - h_n = 0)$. The small cells that fail that condition are made solid $(1 - h_n = 1)$. The Heaviside filter is then applied to the material indicator value ϕ eliminating some of the floating members at low density regions. Fig. 11 (a) shows the resulting design. The second step modifies the thicknesses of the features in the $t_{\rm f} \geq 2h_{\rm min}$ region based on the condition that if $\rho > \rho_{\rm th}$ (for a given density threshold ρ_{th}) and $t_f h_n < h_{min}$, then $t_f h_n$ is set equal to h_{min}. Otherwise, the member is removed. The thicker members among the small cells at the center left of the design in Fig. 11 (b) compared to Fig. 11 (a) are visible. The boundaries of the projected design might exhibit gaps for some periodicities. In the third step, this issue is addressed, and the boundaries are preserved. The density distribution is modified by setting regions with $\rho > 0.7$ to 1 and superimposing them on the design in step 2. Consequently, a thick boundary is seen in Fig. 11 (c). In the fourth step, the small regions are filled to guarantee manufacturability and improve structural performance. For this effect, the analog lattice is thresholded with h_{min} and superimposed on the design from the previous



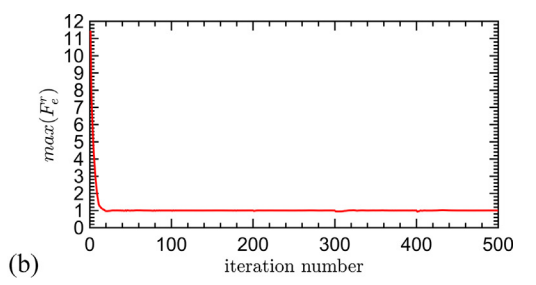


Fig. 8. (a) Volume fraction and (b) maximum failure index convergence histories for the design shown in Fig. 9 (a).

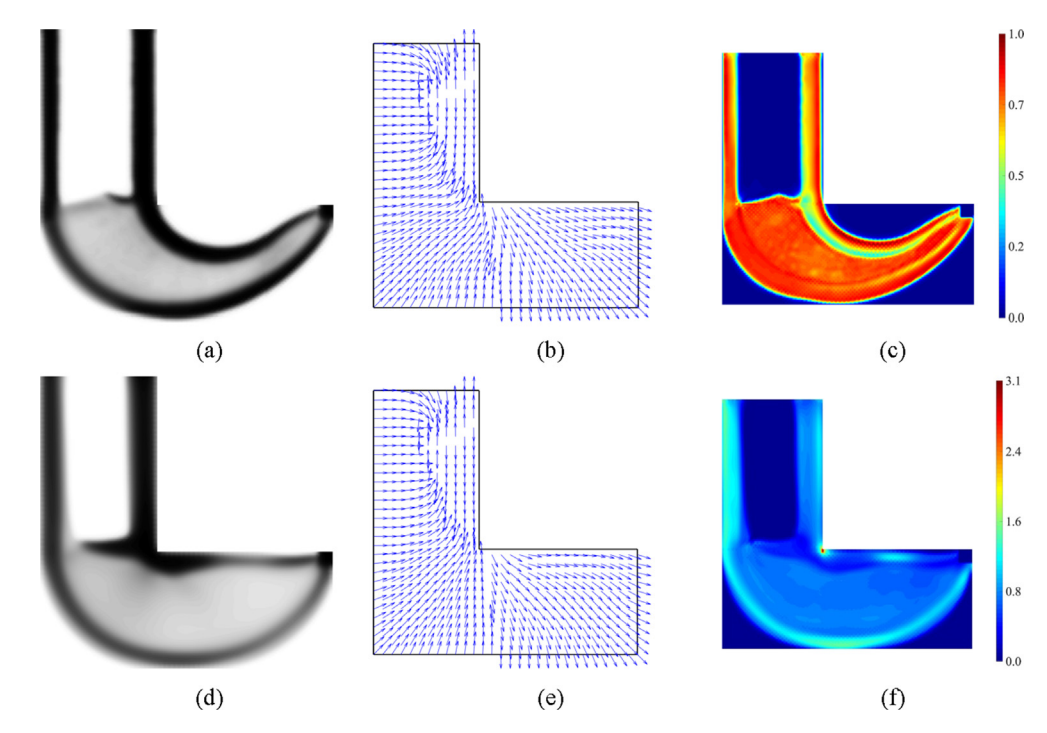


Fig. 9. Optimized stress-constrained design: (a) material distribution; (b) orientation; and (c) failure index (F_e^r) . Optimized compliance-based design: (d) material distribution; (e) orientation; and (f) failure index (F_e^r) .

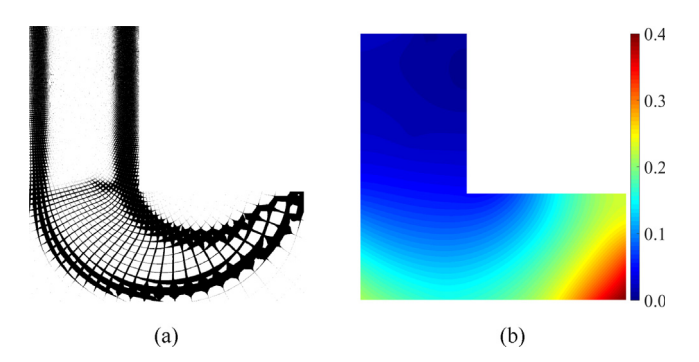


Fig. 10. The projected (a) stress-constrained design and (b) feature size for $\Lambda=0.065$.

step (Fig. 11 (c)). The complement of the superposition is partitioned into regions. Regions for $ho>
ho_{\mathrm{th}}$ with inscribed circles smaller than h_{min} of the diameter are filled. This produces the shape shown in Fig. 11 (d). In the last step, the closed holes inside the design are filled temporarily and their complement is divided into two regions: the solid and void. The shapes of these regions are created using Delaunay triangulation. Adjusting the triangulation factor produces smoother boundaries and exposes vertices inside the boundaries of the regions. These vertices are added to the regions, eliminating floating members. The complement of the shape is taken and the interior holes remain unfilled (Fig. 11 (e)). Several iterations might be required to remove all of the floating members. To produce a smoother shape, the boundary points created using a non-uniform rational basis spline (NURBS) are added to the projected design. Finally, the projected design is imported into MeshLab and is further smoothed using Taubin Filtering with 45 smoothing steps (Fig. 11 (f)). As will be shown later, the outlined post-processing may increase the volume of the optimized structure.

In addition to the stress-constrained design with $\Lambda = 0.065$ (Fig. 11 (f)), the post-processed projected stress-constrained design

with a larger periodicity ($\Lambda=0.13$) is obtained and shown in Fig. 12 (a). The post-processed projected compliance-based design with $\Lambda=0.065$ is also shown in Fig. 12 (b). The post-processed projected designs are analyzed using ANSYS for the same loading and constraint conditions as the optimization model. The failure index for the three designs is shown in Fig. 13 (a)-(c). The small cells in the stress-constrained design for $\Lambda=0.065$ produce a more uniform stress distribution than those in the design for $\Lambda=0.13$. The maximum stresses of the projected stress-constrained designs are distributed over the central boundary of the L-shape. In contrast, the compliance-based design has a high stress concentration at the sharp middle corner that leads to premature yield. The results demonstrate the effectiveness of stress-constrained optimization.

The compliance and failure indexes are reported in Table 5. Upon comparing Table 5 to Table 4, it is observed that post-treatment decreases the compliance by 29% and 25% for the stress-constrained and compliance-based designs, respectively. This difference is explained by the 17% and 26% increases in the volume fractions of the stress-constrained and compliance-based designs, respectively.

6. Experimental evaluation of lattice structures and solid isotropic materials with penalization designs

The second test case considered in this research is the single-edge notched bend problem. Figure 14 shows the dimensions and boundary conditions of the SENB test case. The thickness of the structure is 20 mm. The notch causes stress concentration at its tip. The distributed load ($F=240\ N/mm$) is applied over 6 mm in the middle of the top surface. A region with an area of $12\times 6\ mm^2$ near the applied load is excluded from the design domain. The domain is discretized using 62,580 elements. A length parameter of $r_f=3\ mm$ is selected. As in the previous case, the maximum of the projection parameter is $\beta=r_f/\sqrt{3}l_e$ with $l_e=0.04$, and ten regional stress constraints and a p-mean param-

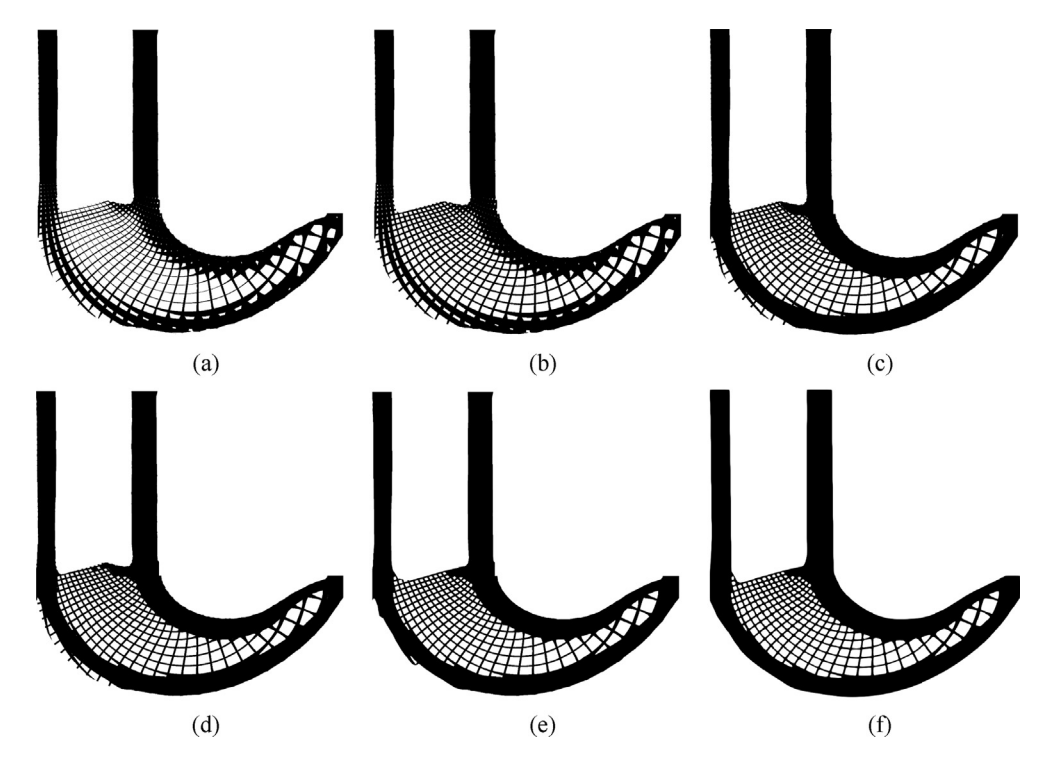


Fig. 11. Projected design: (a) after implementing the minimum feature size; (b) after increasing the thicknesses of members where $\rho > \rho_{th}$; (c) after superposing the density boundary; (d) after small regions have been filled; (e) without floating members; and (f) with smoothed boundaries.

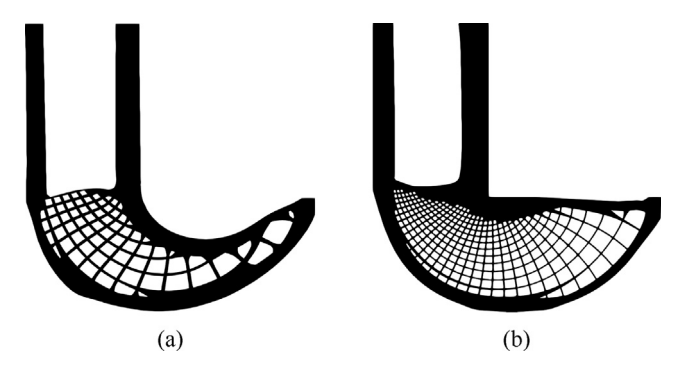


Fig. 12. Post-processed projected designs produced via (a) stress-constrained optimization with $\Lambda=0.13$ and (b) compliance-based optimization with $\Lambda=0.065$.

eter of p=10 are selected. The optimized material distributions for the compliance-based and stress-constrained designs are shown in Fig. 15, and the corresponding volume fraction, specific stiffness, and yield load are reported in the homogenized design section of

Table 6. The reported effective specific stiffness (K_{eff}) is obtained from $K_{eff} = \frac{F}{V_c \delta}$, where δ is the deflection at the top region where the load (F) is applied. The post-processed lattice structures are shown in Fig. 16 (a) and (c). The minimum manufacturable feature size is $h_{min} = 0.8$ mm. Some of the small holes in the postprocessed designs are filled and the walls thickened to comply with the minimum manufacturable feature size. This leads to a considerable increase in the volume fraction (Vg) as reported in the projected design section of Table 6. The effective stiffnesses and yield loads for the projected designs are also reported in Table 6. As shown in the table, in the case of the compliancebased design, the specific stiffnesses of the homogenized and projected designs differ by 15.6% because the projected model has a larger volume fraction that reduces the specific stiffness considerably. The increased volume has a less adverse effect on the specific stiffness of the stress-constrained design.

The test case is also optimized using a solid isotropic material with penalization (SIMP) method. In SIMP, the elastic modulus is related to the density using a power law in order to penalize the intermediate density and restrict the design space to obtain a

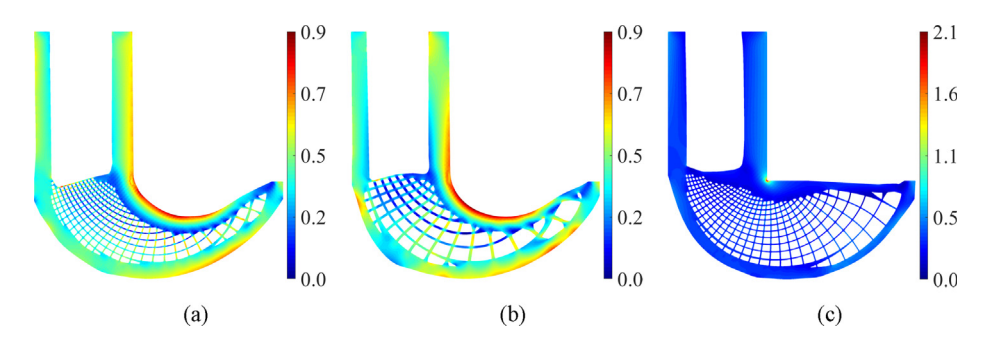


Fig. 13. Failure indexes for the three optimized designs: (a) a stress-constrained optimized design with $\Lambda = 0.065$; (b) a stress-constrained optimized design with $\Lambda = 0.13$; and (c) a compliance-optimized design with $\Lambda = 0.065$.

Table 5The volume fraction, compliance, and failure index for post-treated L-bracket designs.

Designs	V_f	SE (Ncm)	$\max(F_e)$
Stress-constrained, $\Lambda = 0.065$	39.2	20	0.9
Stress-constrained, $\Lambda = 0.13$	39.4	20	0.9
Compliance-based, $\Lambda = 0.065$	42.3	15	2.1

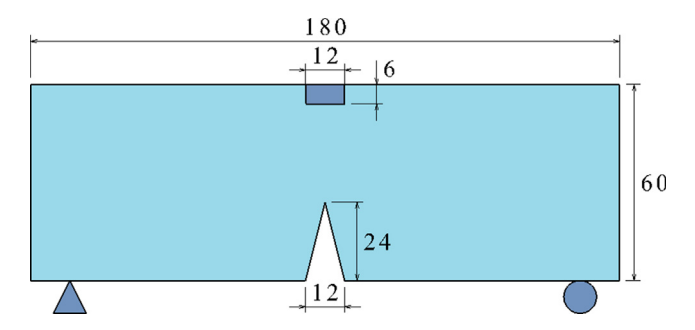


Fig. 14. The SENB test case with dimensions in mm.

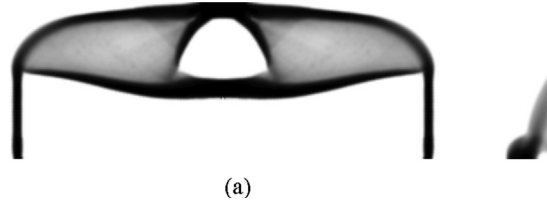
solid-void design. Details of the SIMP method with stress constraint implementation are discussed in Ref. [8]. A compliance-based design and a stress-constrained design were generated using the SIMP topology optimization. The SIMP designs are shown in Fig. 16 (e) and (g). The volume fractions, effective stiffnesses, and yield loads of the SIMP designs are reported in Table 7.

Figure 16 shows the failure index distribution for a load of 1440 N. As in the optimization model, the region near the load application (blue rectangle) is neglected in the stress analysis. Concentrated stress is eliminated in the stress-constrained models, which exhibit more uniform stress distributions throughout the structure. The stresses on the SIMP stress-constrained design (Fig. 16 (f)) are uniformly high throughout the structure, while the lattices in its homogenized counterpart (Fig. 16 (b)) seem to provide low stress and good load transfer from load application to support through the solid regions. The latter design exhibits

high stresses mostly at the bottom bulky region and the inner sides of its legs. The compliance-based designs yield considerably sooner than the stress-constrained designs due to high localized stresses in the notch and at the inner sides of the legs (Fig. 16 (d) and (h)). These results are expected since the stress constraint is not implemented in the compliance optimization approach. The homogenization-based, compliance-based design also exhibits significantly high stresses on its thin, outer members (Fig. 16 (d)) since they are quite thin and play an important role in transferring the load to the supports.

Three specimens for each optimized configuration were additively manufactured using a PA12 printer with multi jet fusion (MJF) technology. The models were tested experimentally in an MTS system with a 50 kN load cell. Three modifications are introduced to the designs to make them experimentally reliable (see Fig. 17 (a), (c), (e), and (g). To allow more surface area for the roller constraints and prevent the supports from sliding off the rollers. the lower supports are extended. The first set of tests reveals that the top of the model tends to slide off to the side (Fig. 18). To address this rigid translation, a semi-circular crown is added such that the top roller can fit inside while remaining as centered as possible throughout the test. The described modifications are responsible for the increased volume fractions among the printed designs in Table 6 and Table 7. Due to these alterations, Table 6 and Table 7 distinguish between optimized and printed models. It is also observed that the support legs, especially those of the stress-constrained designs, rotate too easily as the load increases. Thus, the models fail to reproduce the desired boundary conditions. A thick aluminum plate is placed between the parts and the support rollers, as shown in Fig. 17. However, the homogenization-based, compliance-based design is tested without the plate since the portion of its bottom region near the constraints is low and would hit the plate at high loads. For these reasons, a rotation was verified for this sample, as will be discussed later.

The displacements were measured using DIC. Symmetry was assumed and the two DIC cameras were focused on one side of the structure to magnify the field of view and increase the resolution. This was especially important for lattice structures with smaller members. Figure 19 (a) shows the applied force per volume



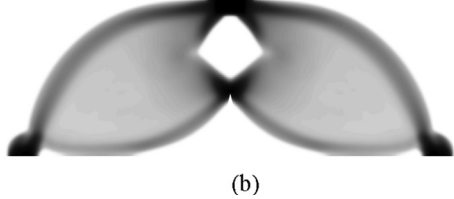


Fig. 15. Optimized (a) stress-constrained and (b) compliance-based designs.

Table 6 Yield loads (F) and stiffnesses (K_{eff}) for homogenization-based designs.

Designs	Optimized Design			Printed Design		
	Homogenized design	FEA for projected design	% diff	FEA	Experim.	% diff
Homogenization-b	ased, stress-constrained design					
V_g	22.9%	28.0%		30.4%	30.4%	
F(N)	1440	1440	0.00	1350.00	1451.05	7.22
$\delta(mm)$	3.30	2.72	19.27	2.43	2.39	1.29
$K_{eff}(N/mm) \\$	1905.52	1890.76	0.78	1831.37	1993.95	8.50
Homogenization-b	ased, compliance-based design					
$V_{\rm f}$	22.9%	28.5%		29.7%	29.7%	
F(N)	360.00	370.18	2.79	420.00	415.00	1.20
$\delta(mm)$	0.63	0.60	3.40	0.72	0.78	6.95
$K_{eff}(N/mm)$	2515.28	2151.57	15.59	1949.77	1797.12	8.15

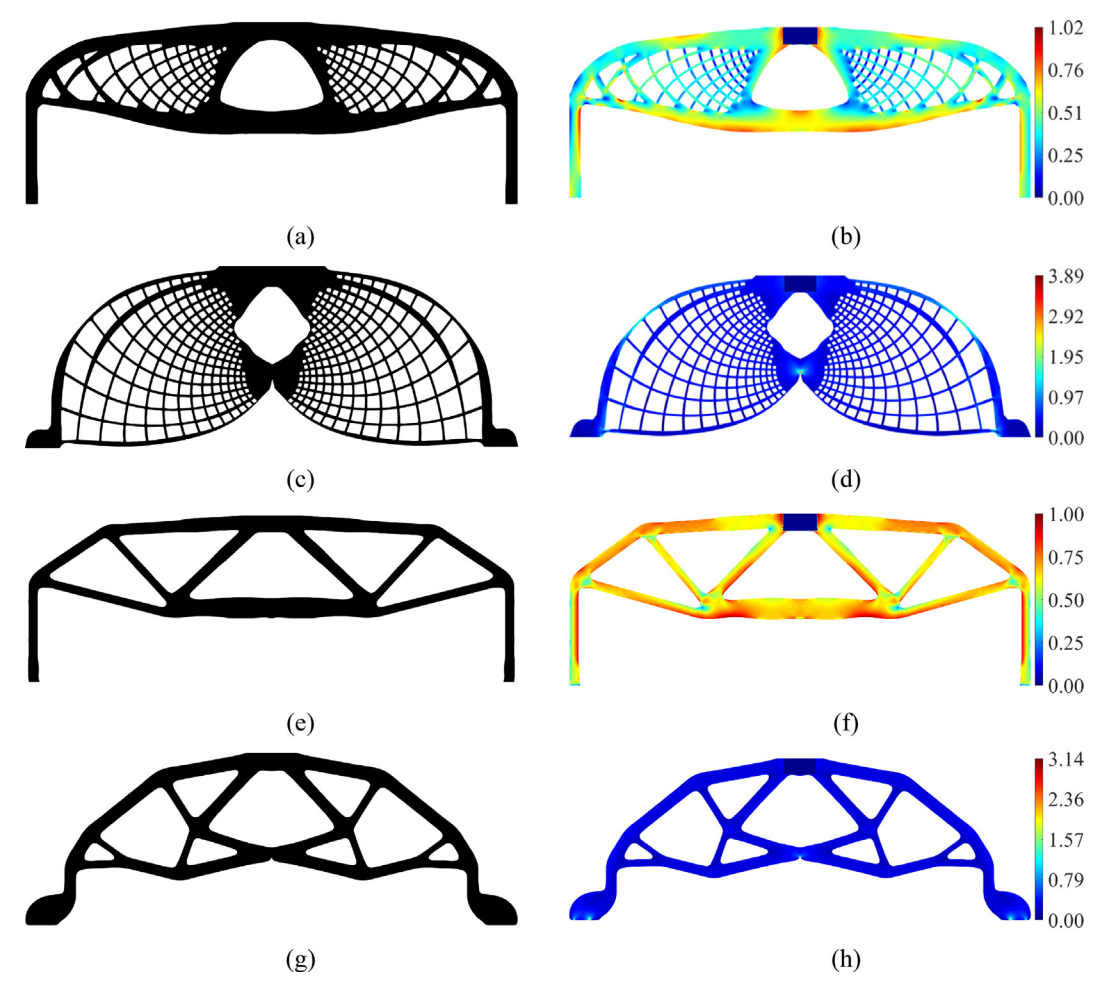


Fig. 16. SENB-optimized designs and failure index distributions at 1440 N: (a) and (b), the homogenization-based stress-constrained design; (c) and (d), the homogenization-based compliance-based design; (e) and (f), the SIMP stress-constrained design; and (g) and (h), the SIMP compliance-based design.

Table 7 Yield loads (F) and stiffnesses (K_{eff}) for SIMP designs.

Designs	Optimized Design	Printed Design		
	FEA	FEA	Experim.	% diff
SIMP stress-constrained d	esign			
V_f	19.9%	22.1%	22.1%	
F(N)	1440.00	1425.00	1360.00	4.67
$\delta(mm)$	3.52	3.35	3.21	4.26
$K_{eff}(N/mm) \\$	2056.77	1924.17	1916.31	0.41
SIMP compliance-based de	esign			
V_f	21.8%	24.6%	24.6%	
F(N)	458.60	590.00	645.00	8.91
$\delta(mm)$	0.87	0.86	0.83	3.62
$K_{eff}(N/mm)$	2432.96	2786.93	3159.03	12.52

fraction versus the vertical displacement per unit of structure height (H) for the four samples. The yield loads (F) for the experimental evaluations reported in Table 6 and Table 7 are determined from the 0.2% offset line of the curve presented in Fig. 19 (a).

The experimental and computational displacement contours at yield are shown in Fig. 19 (b)-(i). The two sets of contours for each design are in good agreement and the computational model predicts a slightly higher maximum displacement than is observed experimentally. However, the homogenization-based, compliance-based design seems to be an exception. For this model, the experimental displacements are higher than the computational displacements. This might indicate that the real model is less con-

strained and rotates more than is predicted via FEA. Another reason for this discrepancy might be that bending of the real sample is not perfectly symmetric.

As shown in the printed design computational and experimental results in Table 6, the homogenization-based, stress-constrained design exhibits an enhanced yield load compared to the compliance-based design. Both the yield load and specific stiffness for the stress-constrained design are similar to those of the homogenized and projected designs. Overall, this design provides a higher ultimate strength than the other three designs (Fig. 19 (a)). As the load increases, some of its thin walls deflect, buckle, and ultimately break (Fig. 17 (b)). The homogenization-based,



Fig. 17. Designs produced via additive manufacturing: the homogenization-based, stress-constrained design (a) before and (b) after testing; the homogenization-based, compliance-based design (c) before and (d) after testing; the SIMP stress-constrained design (e) before and (f) after testing; and the SIMP compliance-based design (g) before and (h) after testing.



Fig. 18. A three-point bending test showing a sample sliding off the rollers.

compliance-based design has the lowest stiffness and strength of the four designs. It exhibits high plasticity and deforms considerably before some of its thin members buckle (Fig. 17 (d)). Although the computational model exhibits some deformation among the thin walls, it predicts yield due to a high stress concentration at the point where the bottom supports touch the rollers. This design has low stiffness because its supports rotate (see Fig. 17 (d)) since

no plate is used. FEA of the homogenization-based, compliance-based design shows that the stiffness would be closer to that of the SIMP compliance-based design (2678.5 N/mm instead of the 1949.8 N/mm shown in Table 6) if no rotation was allowed. This demonstrates that similar specific stiffnesses can be achieved using the SIMP and homogenization methods for the same boundary conditions.

Upon comparing the printed design experimental and computational results reported in Table 6 and Table 7, it can be seen that the stress-constrained lattice and SIMP designs exhibit similar specific stiffnesses. Both the experimental (Fig. 17 (f)) and computational models of the SIMP stress-constrained design demonstrate yield due to bending. The specific stiffnesses of the two models are in good agreement and differ by less than 1%. Experimentally, the model deflects more on one side (Fig. 17 (f)) despite the effort made to center it during test preparation. Comparison of the printed and optimized models in Table 7 indicates similar specific stiffnesses and yield loads. This occurs because the supports are thin and compliant and extending them for testing did not produce significant effects.

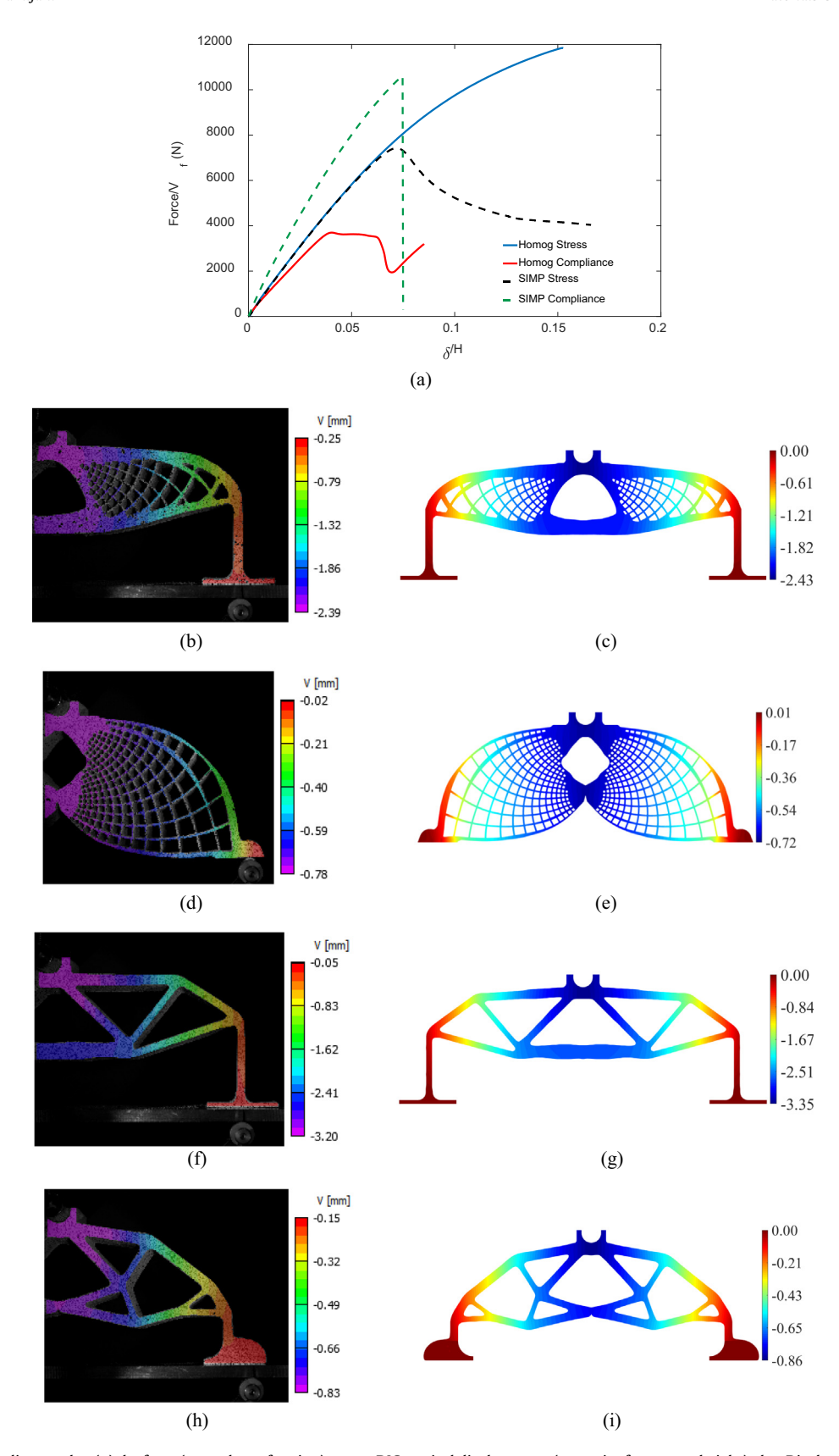


Fig. 19. Three-point bending results: (a) the force (per volume fraction) versus DIC vertical displacement (per unit of structure height) plot. Displacement contour plots [mm] for the: (b) experimental and (c) computational homogenization-based, stress-constrained design; (d) experimental and (e) computational homogenization-based, compliance-based design; (f) experimental and (g) computational SIMP stress-constrained design; and (h) experimental and (i) computational SIMP compliance-based design.

The experimental and computational SIMP compliance-based designs yield expectedly due to high stress concentrations at the notch as the load increases (Fig. 17 (h)). The bulky bottom supports provide more stability and better load bearing, resulting in better stiffness than other models, especially relative to the stressconstrained designs in which the long, thin supports tend to buckle. The FEAs of the printed and optimized designs indicate that the modifications made to the SIMP compliance-based design to make it testable affect its yield load and stiffness. The experimental model is 13% stiffer than computationally predicted. This might indicate that the boundary conditions applied in the FEA model do not fully resemble the real boundary conditions. That is, the aluminum plate provides a much stiffer contact than predicted computationally. The printed designs also have higher yield loads since their bulky supports become even stronger when additional material is added.

Overall, the experimental and computational models are in good agreement with the maximum 12.5% difference in the stiffness of the SIMP compliance-based design. This difference can be attributed to the difficulty of applying perfectly symmetric constraints and loading conditions experimentally and the difficulty of reproducing the experimental boundary conditions via FEA.

7. Conclusions

The implementation of stress constraints in topological and orientation optimization of lattice structures was discussed in this article. The effective properties were calculated using the numerical homogenization method. The results were validated experimentally and then utilized in the optimization algorithm. Compliance-based and stress-constrained optimization algorithms were developed and homogenized designs were obtained. These designs were projected to generate optimized lattice structures. An advantage of the de-homogenization methodology is that optimization can be performed efficiently using a coarse mesh and high-resolution lattice structures can be obtained via projection onto a fine mesh. Two case studies were considered to demonstrate the feasibility of the proposed method. For the first case, the L-shaped bracket, it was observed that the implementation of stress constraints during the optimization process resulted in removal of material at the re-entrant corner and a more uniform failure index distribution. For the SENB test case, the homogenization-based stress-constrained and compliance-based designs were compared to those obtained using SIMP. The two stress-constrained designs exhibited similar structural performance; the two designs had similar stiffnesses and yield strength. Comparison to the compliance-optimized design indicated that stress-constrained optimization is effective in inhibiting yield but compromises stiffness. Experimental evaluation of the optimized designs showed that the additively manufactured models could reach the yield strength determined via the optimization algorithm. However, the experimental results also demonstrated the adverse effects of enforcing a minimum manufacturable feature size. This increases the volume fraction and thus decreases the specific stiffnesses of the lattice structures.

Both the computational and experimental results indicate the importance of including buckling constraints in future studies. As shown in the SENB compliance-based design, thin members are susceptible to buckling. Depending on the minimum member thickness, this may occur before the yield stress is reached. Another important observation is that while we did not intend to obtain coated structures with infill lattices, the optimized designs resemble them due to the use of a minimum manufacturable feature size and a material indicator variable to address stress singularities. The implementation of stress constraints to obtain coated

structures and comparison of their performances to those reported in this article is the subject of future research. Future research also includes extension of this framework to 3D lattice structure designs.

Declaration of Competing Interest

The authors declare that they have no known competing financial interests or personal relationships that could have appeared to influence the work reported in this paper.

Acknowledgements

The authors gratefully acknowledge the support of the National Science Foundation (NSF) under award number 1847133 with program manager Dr. Kathryn Jablokow. The authors also thank Professor Alberto Mello for the help he provided for the experimental evaluations of the optimized design.

Data availability

The data that support the findings of this study are available on request from the corresponding author, AYT.

References

- O. Pantz, K. Trabelsi, A post-treatment of the homogenization method for shape optimization, SIAM J. Control Optim. 47 (3) (2008) 1380–1398.
- [2] J.P. Groen, O. Sigmund, Homogenization-based topology optimization for highresolution manufacturable micro-structures, Int. J. Numer. Meth. Eng. (2017).
- [3] G. Allaire, P. Geoffroy-Donders, O. Pantz, Topology optimization of modulated and oriented periodic microstructures by the homogenization method, Comput. Math. Appl. 78 (7) (2019) 2197–2229.
- [4] P. Duysinx, M.P. Bendsøe, Topology optimization of continuum structures with local stress constraints, Int. J. Numer. Meth. Eng. 43 (8) (1998) 1453–1478.
- [5] G. Rozvany, J. Sobieszczanski-Sobieski, New optimality criteria methods: forcing uniqueness of the adjoint strains by corner-rounding at constraint intersections, Struct. Optimiz. 4 (3-4) (1992) 244-246.
- [6] R. Yang, C. Chen, Stress-based topology optimization, Struct. Optimiz. 12 (2–3) (1996) 98–105.
- [7] P. Duysinx, O. Sigmund, New developments in handling stress constraints in optimal material distribution, in: 7th AIAA/USAF/NASA/ISSMO symposium on multidisciplinary analysis and optimization, 1998, p. 4906.
- [8] C. Le, J. Norato, T. Bruns, C. Ha, D. Tortorelli, Stress-based topology optimization for continua, Struct. Multidiscip. Optim. 41 (4) (2010) 605–620.
- [9] E. Holmberg, B. Torstenfelt, A. Klarbring, Stress constrained topology optimization, Struct. Multidiscip. Optim. 48 (1) (2013) 33–47, https://doi. org/10.1007/s00158-012-0880-7.
- [10] L. Cheng, J. Bai, A.C. To, Functionally graded lattice structure topology optimization for the design of additive manufactured components with stress constraints, Comput. Meth. Appl. Mech. Eng. 344 (2019) 334–359, https://doi.org/10.1016/j.cma.2018.10.010.
- [11] H. Yu, J. Huang, B. Zou, W. Shao, J. Liu, Stress-constrained shell-lattice infill structural optimisation for additive manufacturing, Virt. Phys. Prototyp. 15 (1) (2020) 35–48.
- [12] P.G. Donders, Homogenization method for topology optmization of struc-tures built with lattice materials, 2018.
- [13] K. Gharibi, A.Y. Tamijani, Load-Path-Based Topology Optimization of Two-Dimensional Continuum Structures, AIAA J. (2021) 1–10.
- [14] A.Y. Tamijani, K. Gharibi, M.H. Kobayashi, R.M. Kolonay, Load paths visualization in plane elasticity using load function method, Int. J. Solids Struct. 135 (2018) 99–109, https://doi.org/10.1016/j.ijsolstr.2017.11.013.
- [15] A.Y. Tamijani, S.P. Velasco, L. Alacoque, Topological and morphological Design of Additively-Manufacturable Spatially-Varying Periodic Cellular Solids, Mater. Des. (2020) 109155.
- [16] J. Guedes, N. Kikuchi, Preprocessing and postprocessing for materials based on the homogenization method with adaptive finite element methods, Comput. Meth. Appl. Mech. Eng. 83 (2) (1990) 143–198.
- [17] B. Hassani, E. Hinton, A review of homogenization and topology optimization I—homogenization theory for media with periodic structure, Comput. Struct. 69 (6) (1998) 707–717.
- [18] E. Andreassen, C.S. Andreasen, How to determine composite material properties using numerical homogenization, Comput. Mater. Sci. 83 (2014) 488–495.
- [19] S.J. Hollister, N. Kikuchi, A comparison of homogenization and standard mechanics analyses for periodic porous composites, Comput. Mech. 10 (2) (1992) 73–95.

- [20] J.K. Guest, J.H. Prévost, T. Belytschko, Achieving minimum length scale in topology optimization using nodal design variables and projection functions, Int. J. Numer. Meth. Eng. 61 (2) (2004) 238–254.
- [21] V.S. Deshpande, N.A. Fleck, M.F. Ashby, Effective properties of the octet-truss lattice material, J. Mech. Phys. Solids 49 (8) (2001) 1747–1769.
- [22] G. Sved, Z. Ginos, Structural optimization under multiple loading, Int. J. Mech. Sci. 10 (10) (1968) 803–805, https://doi.org/10.1016/0020-7403(68)90021-0.
- [23] J.P. Groen, J. Wu, O. Sigmund, Homogenization-based stiffness optimization and projection of 2D coated structures with orthotropic infill, Comput. Meth. Appl. Mech. Eng. 349 (2019) 722–742, https://doi.org/10.1016/j. cma.2019.02.031.
- [24] L. Alacoque, R.T. Watkins, A.Y. Tamijani, Stress-based and robust topology optimization for thermoelastic multi-material periodic microstructures, Comput. Meth. Appl. Mech. Eng. 379 (2021), https://doi.org/10.1016/j. cma.2021.113749 113749.
- [25] F.C. Stutz, J.P. Groen, O. Sigmund, J.A. Bærentzen, Singularity aware dehomogenization for high-resolution topology optimized structures, Struct. Multidiscip. Optim. 62 (5) (2020) 2279–2295, https://doi.org/10.1007/s00158-020-02681-6.
- [26] K. Svanberg, The method of moving asymptotes—a new method for structural optimization, Int. J. Numer. Meth. Eng. 24 (2) (1987) 359–373.

- [27] S.G. Johnson, The NLopt nonlinear-optimization package. http://github.com/ stevengi/nlopt.
- [28] F. Hecht, O. Pironneau, freefem+, 2013.
- [29] B.S. Lazarov, O. Sigmund, Filters in topology optimization based on Helmholtztype differential equations, Int. J. Numer. Meth. Eng. 86 (6) (2011) 765–781.
- [30] F. Wang, B.S. Lazarov, O. Sigmund, On projection methods, convergence and robust formulations in topology optimization, Struct. Multidiscip. Optim. 43 (6) (2011) 767–784.
- [31] A. Clausen, E. Andreassen, On filter boundary conditions in topology optimization, Struct. Multidiscip. Optim. 56 (5) (2017) 1147–1155, https:// doi.org/10.1007/s00158-017-1709-1.
- [32] B.S. Lazarov, F. Wang, O. Sigmund, Length scale and manufacturability in density-based topology optimization, Arch. Appl. Mech. 86 (1–2) (2016) 189– 218, https://doi.org/10.1007/s00419-015-1106-4.
- [33] G.A. Da Silva, N. Aage, A.T. Beck, O. Sigmund, Large scale three-dimensional manufacturing tolerant stress-constrained topology optimization, Int. J. Numer. Meth. Eng. 122 (2) (2021) 548–578, https://doi.org/10.1002/ nme 6548
- [34] R.C. Rumpf, J. Pazos, Synthesis of spatially variant lattices, Opt. Express 20 (14) (2012) 15263–15274.
- [35] J. Groen, F. Stutz, N. Aage, J.A. Bærentzen, O. Sigmund, De-homogenization of optimal multi-scale 3D topologies, arXiv preprint arXiv:1910.13002, 2019.